RSC Advances

PAPER

View Article Online
View Journal | View Issue

Cite this: *RSC Adv.*, 2025, **15**, 17491

Biochar-mediated carbon nitride and covalent organic framework photocatalyst for enhanced tetracycline degradation†

Qi Wei,[a] Baojun Yi,[*ab] Zewen Hua,[a] Zhengshuai Sun[a] and Feng Guo[a]

The accumulation of tetracycline (TC) poses a significant challenge to human health and ecological systems. Photocatalytic degradation of TC has been a focus of research, heterojunctions receiving particular attention due to their superior charge separation and transfer properties. This study explores the structural characteristics of heterojunctions and their efficacy in degrading TC in aqueous solutions. We synthesized various combinations of biochar (BC), carbon nitride (CN), and covalent organic frameworks (COF) to form heterojunctions and characterized their morphological, structural, and optical properties using SEM, XRD, XPS, and UV-Vis DRS. These analyses helped elucidate the mechanisms underlying TC degradation. The CN_{10}/COF_2-12, synthesized *in situ*, showed significantly improved degradation efficiency, outperforming CN-10 and COF-2 by factors of 2.02 and 1.96, respectively. Furthermore, the all-solid-state *Z*-scheme heterojunction photocatalyst BC_{10}–CN_{10}/COF_2-22, in which BC serves as the electron mediator, achieved a 3.13-fold increase in TC degradation compared to BC_{10}–CN_{10}-20. The BC-mediated all-solid-state *Z*-scheme heterojunction effectively facilitated the separation and transfer of photogenerated electron–hole pairs. This study combines the advantages of CN, COF, and BC, thereby providing a novel approach to the development of high-performance photocatalysts.

Received 21st March 2025
Accepted 12th May 2025

DOI: 10.1039/d5ra01986a

rsc.li/rsc-advances

1 Introduction

Tetracycline (TC) is a broad-spectrum antibiotic extensively used due to its favorable antimicrobial efficacy and low cost. However, the unregulated overuse of TC has led to significant residues entering water bodies through excretory routes, resulting in water contamination and the spread of antibiotic resistance genes.[1] Therefore, it is crucial to promptly develop effective degradation technologies for TC. Conventional water treatment methods, such as physical adsorption[2] and biological treatment,[3] often fail to completely eliminate TC. In contrast, advanced oxidation processes, particularly photocatalytic technologies,[4,5] show promise in water treatment. These technologies efficiently harness solar energy and convert it into chemical energy under ambient conditions, generating reactive free radicals that facilitate TC degradation.

In the field of photocatalysis, heterostructures have gained significant interest due to their ability to facilitate the separation of photogenerated charge carriers.[6] Particularly, van der Waals (vdW) heterostructures provide a means of bypass the stringent lattice matching demands of epitaxial growth, while enabling precise interfacial control through non-covalent interactions.[7,8] 2D/2D vdW heterojunctions have demonstrated enhanced photocatalytic performance due to their large interfacial area, strong interactions, extended photo-response, and accelerated interfacial charge separation.[9] Compared to 1D–2D and 0D–2D heterostructures, the face-to-face structure offers distinct advantages in increasing interfacial contact area and accelerating charge transfer rates.[10] For example, Qiao *et al.*[11] synthesized a 2D/2D vdW heterostructure of metal-free phosphorene and g-C_3N_4, which demonstrated enhanced efficiency in photocatalytic hydrogen production under visible light. Li *et al.*[8] combined atomically thin g-C_3N_4 with $Bi_9O_{7.5}S_6$ nanoplates to form a 2D/2D vdW heterostructure for CO_2 photoreduction, exhibiting enhanced photocatalytic activity. CN, with its 2D layered structure, suitable band gap, mild synthesis method, and good stability, is ideal for constructing vdW heterostructures.[12–14] COF, a novel class of two-dimensional materials, have potential applications in catalysis, gas storage and optoelectronics due to their structural tunability.[15] They possess excellent specific surface area and tunable structural properties, providing more active sites for photocatalytic reactions. In particular, imine-conjugated COF not only have efficient electron mobility, but also significantly enhance the separation efficiency of photogenerated carriers through the off-domain of π-electrons, thus improving the photocatalytic performance.[16,17] The combination of COF and g-C_3N_4 in a 2D/

[a]*College of Engineering, Huazhong Agricultural University, No. 1, Shizishan Street, Hongshan District, Wuhan, 430070, PR China. E-mail: bjyi@mail.hzau.edu.cn*
[b]*Key Laboratory of Agricultural Equipment in the Mid-lower Yangtze River, Ministry of Agriculture, Wuhan, 430070, PR China*

† Electronic supplementary information (ESI) available. See DOI: https://doi.org/10.1039/d5ra01986a

2D vdW heterojunction is important for the photocatalytic degradation of pollutants. Luo *et al.*[18] modified g-C_3N_4 with COF for imine bonding, preparing β-ketoamine-bonded COF:TP–TTA@g-C_3N_4 with hydrogen production up to 10.1 mmol g^{-1} h^{-1}, significantly enhancing the visible photocatalytic hydrogen evolution performance of g-C_3N_4. Wang *et al.*[19] prepared a novel vdW heterojunction composite combining g-C_3N_4 with COF in nitrogen vacancies, which exhibits an effective interfacial contact area and excellent photocatalytic CO_2 reduction performance. Furthermore, the efficacy of composites in applications is significantly influenced by the preparation methods. For instance, Liu *et al.*[20] demonstrated the *in situ* synthesis of chalcogenides on imide-based COF, which enhanced the stability of chalcogenides and the crystallinity of COF. Wang *et al.*[21] prepared $CsPbBr_3$/CTF-1 composites by electrostatic self-assembly with a simple mechanical stirring method. This invented a covalent triazine framework, which enhanced the efficiency of visible light harvesting and CO_2 photoreduction activity.

However, due to interface resistance, the interface contact of these binary composites is poor, which reduces the transfer efficiency of photogenerated electrons.[22] Therefore, conductive solid electronic dielectrics, such as metal nanoparticles, graphene, and nanocarbon, are incorporated to facilitate carrier transfer.[23] For example, Liu *et al.*[24] synthesized the photocatalyst g-C_3N_4/Ag/TiO_2, where Ag nanoparticles were strategically positioned at the g-C_3N_4 and TiO_2 interface to serve as an electron transport bridge, thereby accelerating charge transfer. Jiang *et al.*[25] constructed an all-solid-state *Z*-scheme heterojunction consisting of CN, CNT, and Bi_2WO_6 nanosheets using carbon nanotubes as an electronic mediator. This configuration effectively promoted the separation and transfer of photogenerated charge carriers, thereby enhancing the photocatalytic activity for TC degradation. However, the widespread application of electronic mediators, including heavy metals and carbon nanotubes, is constrained by their high cost. Consequently, BC, which is cost-effective and exhibits excellent adsorption properties, an abundant pore structure, and favorable electrical conductivity and electron storage capacity, was employed as an electronic mediator.[26,27] Ma *et al.*[28] constructed a novel ternary CdS–WPB–g-C_3N_4 heterojunction photocatalyst, using BC as a green electron transport medium to significantly enhance the carrier separation efficiency. They achieved efficient degradation of methyl orange under visible light (99% degradation in 80 minutes) and ultraviolet light (complete degradation in 60 minutes). Furthermore, there are few reports on the use of BC in g-C_3N_4/COF composites or even ternary heterojunctions.

To address the challenges in current photocatalytic systems, this study aims to develop photocatalysts with excellent photocatalytic performance and cost-effectiveness by synergistically integrating the structural and electronic advantages of CN, COF and BC. Specifically, BC is adopted as a sustainable electron transfer medium, which overcomes the limitations of traditional high-cost metal media. A 2D/2D vdW heterostructure is constructed between COF and g-C_3N_4. Through atomic-level π-orbital overlap, the interface charge separation is maximized. These physicochemical and chemical characterization of photocatalysts to reveal the relationship between their structure and photocatalytic performance. The findings provide novel insights for the development of efficient photocatalysts and propose innovative solutions for the effective degradation of TC.

2 Experimental methods

2.1 Materials

TC, dicyandiamide, anhydrous ethanol, sodium chloride, 4,4′,4″-(1,3,5-triazine-2,4,6-triyl)triphenylamine (TTA), 1,3,5-tricarbonylresorcinol (TP), dimethylsulfoxide (DMSO), and methanol were purchased from China National Pharmaceutical Chemical Reagent Co. Wood chips, obtained from Anhui Zhengjie Feed Co., Ltd, China, were passed through a 60-mesh sieve and subsequently dried at 105 °C for 48 h to ensure complete removal of moisture.

2.1.1 Preparation of monolithic photocatalysts. The preparation of BC was achieved through the pyrolysis of 2 g of wood chips under a nitrogen gas flow of 50 mL min^{-1}. The temperature was incrementally raised to 500 °C at a heating rate of 20 °C min^{-1} and maintained for 1 h. The pyrolysis-derived solid product was subsequently cooled to ambient temperature under a nitrogen atmosphere before being collected, yielding black powdery BC.

The preparation of CN involved the dissolution of 4.5 g of dicyandiamide in 500 mL of ethanol. Subsequently, a saturated aqueous solution of sodium chloride was added dropwise to the mixture under constant stirring. The ethanol and water were removed by rotary evaporation, thereby obtaining a solid residue. The residue was then heated for 2 h at 550 °C with a heating rate of 5 °C min^{-1}. After cooling, the product was washed extensively with deionized water and dried at 120 °C to obtain the final CN material.

The preparation of COF was initiated by dissolving 0.07 mmol of TTA and 0.13 mmol of TP in 5 mL of DMSO, followed by sonicated to ensure complete dissolution. The resulting solution was then poured into an autoclave and heated at 120 °C for 12 h. The product was then washed with methanol and subsequently dried at 105 °C, thereby obtaining the COF.[19]

2.1.2 Preparation of photocatalysts with fixed component masses. The masses of BC, CN, and COF were quantified to be 10 mg, 10 mg, and 2 mg, respectively, in order to prepare a fixed monomer mass photocatalyst. A solution containing 82.98 mg of CN in 5 mL of DMSO was prepared and sonicated for 2 minutes to facilitate dispersion. Subsequently, 0.07 mmol of TTA and 0.13 mmol of TP were mixed into the solution, which was then sonicated and mixed again to provide the requisite reaction conditions for the generation of COF. The mixture was heat-treated in an autoclave at 120 °C for 12 h. The product, after being washed with methanol, was designated as CN_{10}/COF_2-12. In the same experimental procedure, CN was replaced with BC to obtain BC_{10}/COF_2-12. The '/' symbol denotes the chemical complexation method.

10 mg of BC and 10 mg of CN were thoroughly stirred under an inert atmosphere, and the product was labeled as BC_{10}–CN_{10}-20. The '–' symbol stands for the physical compounding method.

A solution of 82.98 mg of BC_{10}–CN_{10}-20 in 5 mL of DMSO was prepared and sonicated for 2 minutes to disperse the material. Subsequently, 0.07 mmol of TTA and 0.13 mmol of TP were added, and the solution was sonicated and mixed again to provide the reaction conditions for the generation of COF. The mixture was then heat-treated at 120 °C in an autoclave for 12 h. After this period, the product was washed with methanol and recorded as BC_{10}–CN_{10}/COF_2-22. The synthesis of BC_{10}/COF_2–CN_{10}-22 involved the complete stirring of the reactants under an inert atmosphere. Similarly, the synthesis of CN_{10}/COF_2–BC_{10}-22 entailed the complete stirring of CN_{10}/COF_2-12 and BC under an inert atmosphere. The naming correspondence table of photocatalysts with fixed component masses is shown in Table S1.†

2.1.3 Preparation of photocatalysts with fixed total mass. The mass of the photocatalyst was standardized to 5 mg to ensure a consistent total mass for all preparations. CN_3/COF_2-5 was prepared in a mass ratio of CN to COF of 3 : 2, while BC_3/COF_2-5 was prepared in a mass ratio of BC to COF of 3 : 2, following the preparation method detailed in Section 2.1.2.

The samples, designated as BC_3–CN_3/COF_4-5 and BC_3/COF_3–CN_4-5, were prepared by combining BC, CN, and COF in a mass ratio of 3 : 3 : 4, in accordance with the methodology described in Section 2.1.2. The naming correspondence table of photocatalysts with fixed total mass is shown in Table S2.†

2.2 Adsorption and degradation experiments

A 50 mL of aqueous solution of TC at a concentration of 20 mg L^{-1} was prepared and transferred into a 50 mL reactor. The catalyst was then added, followed by thorough stirring to achieve uniform dispersion throughout the solution. The mixture was continuously stirred for an additional 30 minutes in the dark to establish a dynamic equilibrium between the catalyst and TC molecules. Subsequently, the light source was initiated, with the light intensity adjusted to approximately 7000 Lux to control the photocatalytic reaction rate, thereby facilitating observation and detailed analysis of the reaction process. At regular intervals, 1 mL of the solution was removed and filtered through a 0.45 μm aqueous membrane to eliminate catalyst particles. The concentration of TC in the filtered samples was subsequently quantified using high-performance liquid chromatography (HPLC). Each experiment was independently repeated three times, and the experimental data is presented as the mean, with the coefficient of variation provided in Table S3.†

2.3 Characterization methods

The crystal structures of the samples were analyzed using a Bruker D8 Advance X-ray diffraction (XRD) from Germany. The elemental composition and the chemical bonding states of the photocatalysts were investigated using a Thermo Fisher Scientific Escalab 250Xi photoelectron spectrometer (XPS) from the USA. Microscopic morphology was visualized with a high-resolution, cold field-emission scanning electron microscope (SEM), model Regulus-8100, from Hitachi, Japan. Pore properties were investigated using a Quadrasorb evoTM fully automated specific surface area and porosity analyzer, manufactured by Kantar Instruments, USA. The visible light absorption properties of the photocatalysts were determined using a UV-3600 UV-Vis spectrophotometer from Shimadzu, Japan. Photoluminescence (PL) properties were characterized using a FLS-1000 instrument from Edinburgh Instruments Ltd, UK, with an excitation wavelength of 350 nm. The photoelectric properties were evaluated using a CHI-660E electrochemical workstation from Shanghai Chenhua Instrument Co.

3 Results and discussion

3.1 Photocatalytic degradation performance

3.1.1 Photocatalytic performance of mono- and binary photocatalysts. The photocatalytic performance and light/dark reaction ratios of the monolithic and binary photocatalysts are illustrated in Fig. 1. Fig. 1a shows the adsorption rates of TC on the photocatalysts BC-10, CN-10, COF-2, BC_{10}–CN_{10}-20, BC_{10}/COF_2-12, and CN_{10}/COF_2-12 as 5.94%, 1.8%, 5.77%, 5.86%, 25.53%, and 11.43%, respectively, following a 30 minutes in the dark. The degradation rates of TC on these photocatalysts after 360 minutes of photoreaction were 36.98%, 49.39%, 50.8%, 31.81%, 97.84%, and 99.79%, respectively. The CN_{10}/COF_2-12 demonstrated a significantly higher photocatalytic efficiency compared to CN-10 and COF-2, with ratios of 2.02 and 1.96, respectively. This result is consistent with the mechanism reported in the literature by which vdW heterojunctions enhance photocatalytic activity.[29] Similarly, the BC_{10}/COF_2-12 showed a markedly higher photocatalytic efficiency than BC-10 and COF-2, with enhancements of 2.65-fold and 1.93-fold, respectively. While CN_{10}/COF_2-12 had the best photocatalytic performance, BC_{10}/COF_2-12 had an adsorption capacity 2.22 times higher during the adsorption phase of the dark reaction. However, excessive adsorption may lead to pore blockage of active sites, thereby impeding light penetration and reducing photon utilization efficiency. Notably, the 2D/2D heterojunction formed between CN and COF layers facilitated effective π-electron delocalization, which significantly enhanced the *Z*-scheme charge transfer efficiency and consequently improved the photocatalytic performance. Kinetic analysis indicates (Fig. 1b) that, except for the BC material, the degradation processes of TC by other catalysts all conform to the pseudo-first-order kinetic model ($R^2 > 0.98$). The specific dynamic parameters and linear regression analysis are detailed in Table S3.† In Table S3,† the BC_{10}/COF_2-12 exhibited the most substantial adsorption contribution in the dark reaction, reaching a value of 27%. The BC_{10}–CN_{10}-20 and BC-10 also had significant adsorption contributions of 19% and 17%, respectively. In comparison, the CN-10, COF-2, and CN_{10}/COF_2-12 had lower adsorption contributions of 5%, 8%, and 11%, respectively. Nevertheless, the BC_{10}–CN_{10}-20 showed a markedly diminished catalytic activity compared to individual BC-10 or CN-10. The composite method exerts an influence on the active sites of the catalysts.[30] This phenomenon is postulated to be associated with the manner in which BC and CN are compounded.

3.1.2 Photocatalytic performance of ternary photocatalysts. The photocatalytic performance and light/dark reaction ratios

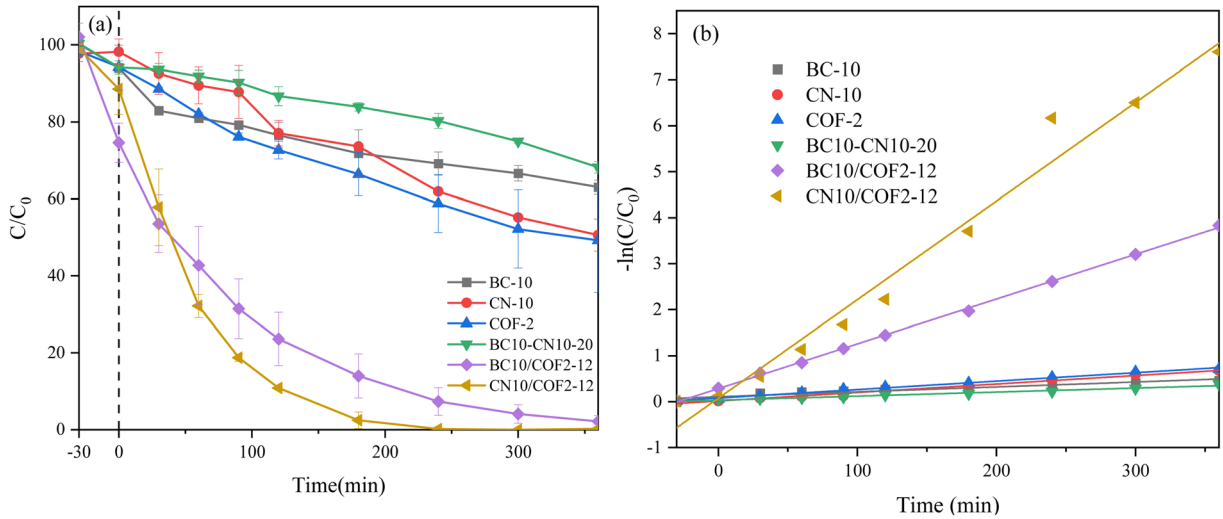

Fig. 1 Single and dual-component photocatalysts: (a) photocatalytic degradation of TC. (b) Kinetic fitting curve.

of the ternary photocatalysts are illustrated in Fig. 2. After a 30 minutes dark reaction, the adsorption rates of TC on BC_{10}–CN_{10}-20, BC_{10}/COF_2-12, CN_{10}/COF_2-12, BC_{10}–CN_{10}/COF_2-22, CN_{10}/COF_2–BC_{10}-22, and BC_{10}/COF_2–CN_{10}-22 were 5.86%, 25.53%, 11.43%, 22.6%, 20.24%, and 17.34%, respectively (Fig. 2a). Following a 360 minutes photoreaction, the degradation rates of TC on these photocatalysts were 31.81%, 97.84%, 99.79%, 99.65%, 99.3%, and 80.53%, respectively. The BC_{10}–CN_{10}/COF_2-22 showed a notable enhancement in catalytic performance compared to BC_{10}–CN_{10}-20, exhibiting a performance increase of up to 3.13 times. However, the photocatalytic effect of BC_{10}/COF_2–CN_{10}-22 was less pronounced than that of BC_{10}/COF_2-12, and CN_{10}/COF_2–BC_{10}-22 performed worse than CN_{10}/COF_2-12. The BC_{10}–CN_{10}/COF_2-22 was optimized for TC degradation efficiency through a dual-stage compounding strategy, starting with physical and followed by chemical compounding. In contrast, BC_{10}/COF_2–CN_{10}-22 and CN_{10}/COF_2–BC_{10}-22, prepared with a chemical followed by physical compounding strategy, showed reduced TC degradation efficiency. It is postulated that the post-physical compounding might result in the formation of an encapsulating layer during the chemical compounding stage, potentially covering active sites and limiting photocatalyst performance enhancement. The sequence of chemical compounding steps during synthesis significantly influences photocatalytic performance, particularly the final chemical compounding of COF. Kinetic analysis indicates (Fig. 2b) that, except for the BC_{10}–CN_{10}/COF_2-22 material, the degradation processes of TC by other catalysts all conform to the pseudo-first-order kinetic model ($R^2 > 0.98$). The specific dynamic parameters and linear regression analysis are detailed in Table S3.† As illustrated in Table S3,† the adsorption contributions of BC_{10}–CN_{10}-20, BC_{10}/COF_2-12, CN_{10}/COF_2-12, BC_{10}–CN_{10}/COF_2-22, CN_{10}/COF_2–BC_{10}-22, and BC_{10}/COF_2–CN_{10}-22 to the overall photocatalytic reaction in the dark were 19%,

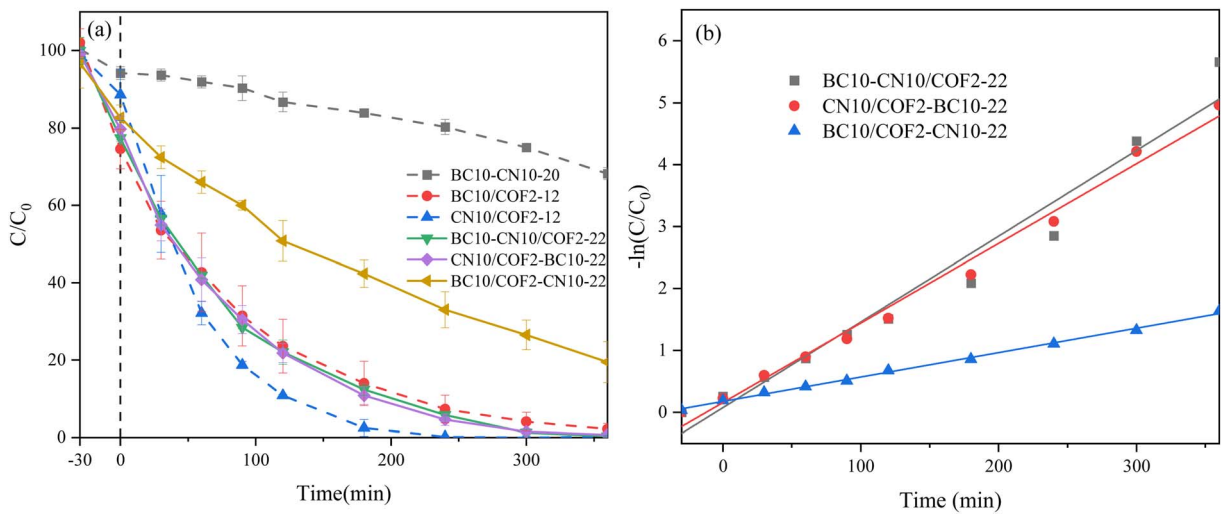

Fig. 2 Three-component photocatalysts: (a) photocatalytic degradation of TC. (b) Kinetic fitting curve.

27%, 11%, 23%, 20%, and 18%, respectively. BC-containing composites exhibited higher adsorption contributions in the dark reaction compared to others. Conversely, CN_{10}/COF_2-12, which lacked BC, demonstrated the lowest adsorption contribution at 11%. It is hypothesized that the presence of BC significantly enhances the adsorption performance of the photocatalysts in the dark reaction.

3.1.3 Photocatalytic performance of quantitative photocatalysts. To ensure the accuracy of photocatalytic performance comparisons, catalyst samples of different systems were prepared in this study with a quantitative mass of 5 mg, which was determined to eliminate the impact of dosage variation on the results. The photocatalytic performance and light/dark reaction ratios of the quantitative photocatalysts are illustrated in Fig. 3. As illustrated in Fig. 3a, after a 30 minutes dark reaction, the adsorption rates of TC on BC_{10}/COF_2-12, CN_{10}/COF_2-12, BC_3/COF_2-5, CN_3/COF_2-5, BC_3/COF_4–CN_3-5, and BC_3–CN_3/COF_4-5 were 25.53%, 11.43%, 9.5%, 8.65%, 6.81% and 12.35%, respectively. After a 360 minutes photoreaction, the degradation rates of TC on these photocatalysts were 97.84%, 99.79%, 86.59%, 86.18%, 87.72%, and 99.65%, respectively. The two ternary photocatalysts, BC_3–CN_3/COF_4-5 and BC_3/COF_4–CN_3-5, exhibited superior photocatalytic performance compared to the binary photocatalysts, BC_3/COF_2-5 and CN_3/COF_2-5. This indicates that ternary photocatalysts have enhanced photocatalytic effects in comparison to binary photocatalysts under quantitative conditions. Moreover, the photocatalytic performance of BC_3–CN_3/COF_4-5 was superior to that of BC_3/COF_3–CN_4-5, confirming that chemical compounding at the final stage of preparation can markedly enhance the overall performance of the photocatalysts. Kinetic analysis indicates (Fig. 3b) that the degradation processes of TC by all catalysts conform to the pseudo-first-order kinetic model ($R^2 > 0.98$). The specific dynamic parameters and linear regression analysis are detailed in Table S3.† As illustrated in Table S3,† the adsorption contributions of BC_{10}/COF_2-12, CN_{10}/COF_2-12, BC_3/COF_2-5, CN_3/COF_2-5, BC_3/COF_4–CN_3-5 and BC_3–CN_3/COF_4-5 to the overall photocatalytic reaction in the dark were 27%, 11%, 8%, 8%, 7%, and 12%, respectively. The data indicate that the proportion of BC in the photocatalyst significantly affects its adsorption performance in the dark reaction.

3.2 Material characterization

3.2.1 Compositional analysis. The XRD patterns of CN, COF, and BC are presented in the accompanying Fig. S1.† For CN, the diffraction peak at approximately 27.5° suggests interlayer stacking on the (002) crystal surface, confirming the presence of a highly graphitic structure.[31] For BC, a more intense peak at 30.9° is characteristic of $CaMg(CO_3)_2$. For COF, no significant peak was observed within the 10–90° range. Subsequent small-angle XRD tests revealed a distinct diffraction peak at 5.8°, corresponding to the (100) plane reflection of the regularly ordered lattice.[32] As illustrated in Fig. 4a, the absence of discernible COF diffraction peaks in the CN_{10}/COF_2-12 composites may be attributed to the relatively low loading content and optimal dispersion of COF on the CN surface. However, by calculating the crystal size through the Scherrer equation,[33] the results show that the average grain size of CN has significantly decreased from 61.1 nm of the original CN to 20.9 nm of the CN_{10}/COF_2-12 composite material. This significant decline strongly indicates that the COF units have successfully combined *in situ* to the CN matrix. The intense and broad diffraction peaks of CN suggest a potential alteration in the interlayer stacking by the doped COF. Comparing the spectra of CN_{10}/COF_2-12 and CN_{10}/COF_2–BC_{10}-22 reveals a notable reduction in the height of the characteristic peaks for CN in the latter, possibly due to BC doping, which can reduce CN crystallinity. Fig. 4b illustrates a shift to a higher angle of 27.7° for the BC_{10}–CN_{10}-20, in comparison to that of the CN, indicating a reduction in layer spacing and tighter bonding at the interfaces.[34] Nevertheless, the diminished height of the corresponding diffraction peaks may be attributed to the mutual coverage between BC and CN in the composites. The

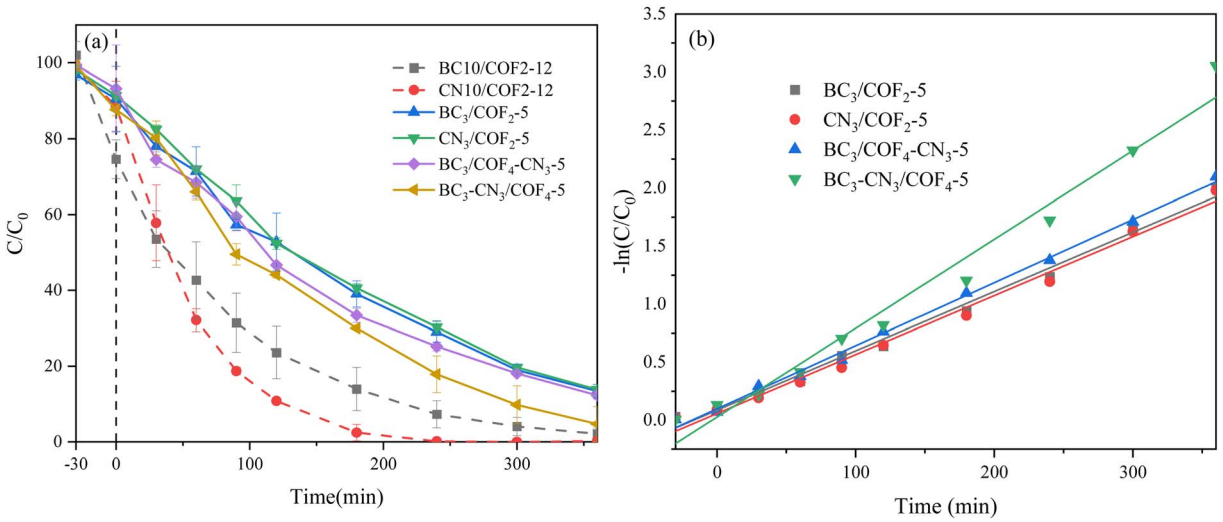

Fig. 3 Quantitative photocatalysts: (a) photocatalytic degradation of TC. (b) Kinetic fitting curve.

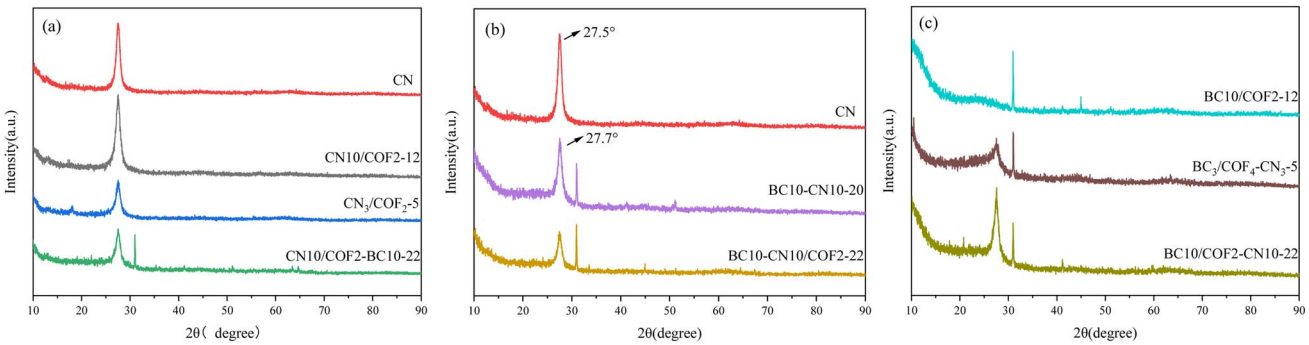

Fig. 4 XRD patterns of photocatalyst: (a) CN, CN_{10}/COF_2-12, CN_3/COF_2-5, and CN_{10}/COF_2–BC_{10}-22, (b) CN, BC_{10}–CN_{10}-20, BC_{10}–CN_{10}/COF_2-22, and (c) BC_{10}/COF_2-12, BC_3/COF_4–CN_3-5, and BC_{10}/COF_2–CN_{10}-22.

peak intensity of the diffraction peak corresponding to CN in the BC_{10}–CN_{10}/COF_2-22 is further diminished, which may be attributed to the formation of a *Z*-scheme heterostructure. This structure might enhance the dispersion of CN through interfacial interactions, as supported by the literature.[35] Fig. 4c shows increased intensity of the CN characteristic peaks in the BC_{10}/COF_2–CN_{10}-22 in comparison to BC_3/COF_4–CN_3-5, likely due to a higher proportion of CN. However, the formation of a thicker encapsulation layer on the surface of the BC_{10}/COF_2-12 material, potentially attributable to an increased number of CN units, may obscure the active sites of the catalysts. This is verified by the experimental result that the photocatalytic efficiency of BC_{10}/COF_2–CN_{10}-22 (80.53%) is lower than that of BC_3/COF_4–CN_3-5 (87.72%).

Fig. 5 depicts the surface elemental composition and chemical forms of the photocatalysts. The N 1s high-resolution spectrum of COF, after fitting, revealed two distinct peaks at 398.2 eV and 399.8 eV, corresponding to the –N=C and –N–C groups, respectively.[36] In CN, three N 1s peaks were observed at 398 eV, 399.5 eV, and 400.6 eV, respectively. The peak at 398 eV is attributed to an aromatic nitrogen carbon atom (C=N–C) hybridized by sp^2 in the triazine ring. The peak at 399.5 eV is assigned to a nitrogen atom in $(N–(C)_3)$, and the peak at 400.6 eV is indicative of the presence of a C–N–H group.[37] For CN_{10}/COF_2-12, these peaks shifted to higher binding energies, suggesting changes in the chemical state or coordination conditions of the N atoms. This shift is proposed to result from electron transfer from CN to COF upon coupling, indicating the formation of an intimate heterojunction between CN and COF.[19] As illustrated in Fig. 5b, the N 1s high-resolution spectrum of BC_{10}–CN_{10}-20 exhibits three fitted peaks at 397.9 eV, 399.4 eV, and 400.5 eV. The peaks at 397.9 eV and 400.5 eV are indicative of the C–N and N–H bonds in the CN triazine ring, respectively. However, the peaks in BC_{10}–CN_{10}-20 are shifted toward lower binding energies, indicating a decrease in electron cloud density and weakened electron binding ability.[38] The characteristic peak of the BC_3–CN_3/COF_4-5, observed at 399.5 eV, is attributed to the –N–C group in COF. This observation suggests that the complexation of BC_{10}–CN_{10}-20 with the COF material results in the formation of the –N–C group. Furthermore, in comparison to the BC_{10}–CN_{10}-20, the characteristic peaks of BC_3–CN_3/COF_4-5 at 398.2 eV and 400.6 eV, exhibiting a shift towards higher binding energies. This phenomenon may be attributed to interfacial charge transfer, which results in the nitrogen atoms experiencing a loss of electron density.[39] It is hypothesized that BC_3–CN_3/COF_4-5 forms a *Z*-scheme heterostructure.

3.2.2 Morphology and pore structure analysis. The morphology of the photocatalyst is illustrated in Fig. S2.† CN displays a reef-like structure composed of numerous interconnected protrusions and depressions, enhancing the material's active sites. The material in Fig. S2b† is composed of small-diameter agglomerated small particles, which is consistent with the morphology of COF in the literature.[40] Its

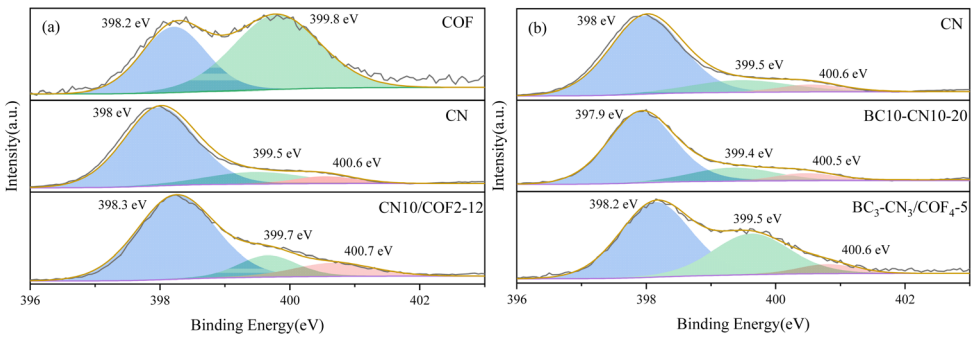

Fig. 5 High-resolution XPS spectra of N 1s in photocatalyst: (a) COF, CN, and CN_{10}/COF_2-12 and (b) CN, BC_{10}–CN_{10}-20, and BC_3–CN_3/COF_4-5.

microstructure reveals a complex, fibrous morphology with discernible hollow spaces. Fig. S2c† illustrates the uniform distribution of COF on the surface of the lamellar structure of CN, confirming efficient deposition of COF on CN nanosheets through π–π interactions to form the CN_{10}/COF_2-12 heterostructure. Furthermore, this intimate interface facilitates charge separation during photocatalysis,[19] which is consistent with the experimental results that the CN_{10}/COF_2-12 has a high photocatalytic degradation efficiency of 99.79%. As illustrated in Fig. S2d,† a lamellar structure of CN is deposited on the BC surface in the BC_3–CN_3/COF_4-5, where COF was uniformly dispersed in BC_{10}–CN_{10}-20.

As illustrated in Fig. S3a,† BC displays a conventional type IV isothermal curve with H4 hysteresis loops, indicative of a uniform pore size distribution. This is attributed to the gradual release of volatiles during the carbonization of the BC at lower pyrolysis temperatures, which contributes to the formation of micropores and a larger specific surface area.[41] With the exception of BC, all other samples display type IV isothermal curves with evident H3 hysteresis loops, indicating pronounced mesoporous structures. The COF material, characterized by a well-ordered crystalline and pore structure, results in a high specific surface area. Additionally, the presence of hollow space within the material contributes to a large total pore volume, as illustrated in Fig. S2b.† The notable enlargement of the pore size in the CN_{10}/COF_2-12 composite enhances the adsorption capacity, although its specific surface area is markedly lower in comparison to the other samples. The lower specific surface area of CN_{10}/COF_2–BC_{10}-22 in comparison to CN_{10}/COF_2-12 can be attributed to the physical agitation approach, causing the formation of particle agglomerates of BC and CN_{10}/COF_2-12, which limits the effective formation of a CN_{10}/COF_2-12 and BC composite. Fig. S3b† illustrates that BC has a considerable abundance of mesopores and a paucity of macropores. In contrast, CN_{10}/COF_2-12 composites display a relatively high proportion of macropores. Consequently, BC_3–CN_3/COF_4-5 composites possess a substantial proportion of both mesopores and macropores, which is conducive to enhanced adsorption capacity. It is particularly emphasized that the presence of macropores plays a beneficial role in the photocatalytic process. In addition to providing more adsorption sites,[42] they also facilitate the mass transfer efficiency of the photocatalytic reaction. In comparison to BC_{10}–CN_{10}/COF_2-22, the proportion of mesopores and macropores in CN_{10}/COF_2–BC_{10}-22 and BC_{10}/COF_2–CN_{10}-22 was significantly diminished, indicating that different preparation techniques significantly affect the pore structure of the samples. The photocatalytic degradation efficiency of CN_{10}/COF_2–BC_{10}-22 (99.3%) and BC_{10}/COF_2–CN_{10}-22 (80.53%) was lower than that of BC_{10}–CN_{10}/COF_2-22 (99.65%), indicating that the presence of mesopores and macropores is favorable for the photocatalytic (Table 1).

3.2.3 Optical performance analysis. The optical properties of the photocatalyst are shown in Fig. 6. Fig. 6a reveals the light absorption properties and spectral characteristics, with the light absorption band edges of 503 nm, 581 nm and 780 nm for CN-10, CN_{10}/COF_2-12, and BC_{10}–CN_{10}/COF_2-22, respectively. In comparison to CN-10, the visible absorption edge of CN_{10}/COF_2-12 exhibited a red shift, accompanied by an expansion of the spectral absorption range. This phenomenon can be attributed to the synergistic and interfacial interactions between CN and COF, which align with the experimental findings. Specifically, the degradation efficiency for TC by CN_{10}/COF_2-12 was enhanced by a factor of 2.02 in comparison to that of CN. The addition of BC resulted in a significant redshift, accompanied by a notable enhancement in visible light absorption intensity for the ternary catalyst BC_{10}–CN_{10}/COF_2-22. The valence band structures were analyzed using Tauc plots (Fig. 6b), and the E_g of CN, CN_{10}/COF_2-12, and BC_{10}–CN_{10}/COF_2-22 were calculated to be 2.67 eV, 2.31 eV, and 2.01 eV, respectively, based on the relationship between $(\alpha h\nu)^2$ and $h\nu$. These values are consistent with literature reports.[43] The findings indicate that CN_{10}/COF_2-12 displays a narrower bandgap, whereas the forbidden bandwidth of BC_{10}–CN_{10}/COF_2-22 is further diminished, extending the visible light absorption range.[44] This due to the formation of an all-solid-state *Z*-scheme heterostructure, which effectively inhibits electron–hole pairs recombination and enhances photocatalytic efficiency. This is supported by the experimental finding that the degradation efficiency of TC by BC_{10}–CN_{10}/COF_2-22 is 3.13 times higher than that of BC_{10}–CN_{10}-20. However, the photocatalytic degradation efficiency of BC_{10}–CN_{10}/COF_2-22 is lower than that of CN_{10}/COF_2-12. This might be because, compared with traditional media, biochar has a lower inherent electrical conductivity, which may hinder the electron transfer between CN and COF. From the VB-XPS plot in Fig. 6c, the VB values of CN and COF were determined to be 1.90 eV and 2.45 eV, respectively, by calculating the *x*-axis intercept. The CB values of CN and COF were calculated using the equation $E_{CB} = E_{VB} - E_g$, resulting in −0.77 eV and 0.52 eV for CN and COF, respectively. Based on the data, the energy band structure of CN_{10}/COF_2-12 is schematically represented in Fig. 6d. The VB-

Table 1 Structure properties of photocatalyst

Sample	S_{BET} ($m^2\ g^{-1}$)	V_{Total} ($cm^3\ g^{-1}$)	V_{Micro}[a] ($cm^3\ g^{-1}$)	V_{Ext}[b] ($cm^3\ g^{-1}$)	$D_{Average}$ (nm)
BC	250.50	0.12	0.02	0.10	1.93
COF	239.56	0.23	0.16	0.07	3.88
CN_{10}/COF_2-12	43.37	0.10	0.09	0.01	9.09
BC_3–CN_3/COF_4-5	131.23	0.18	0.10	0.08	5.37
CN_{10}/COF_2–BC_{10}-22	32.68	0.06	0.05	0.01	7.23
BC_{10}/COF_2–CN_{10}-22	33.22	0.06	0.05	0.01	7.47

[a] Pore volume of micropore, calculated by *t*-plot. [b] Calculated by difference ($V_{Ext} = V_{BET} - V_{Micro}$).

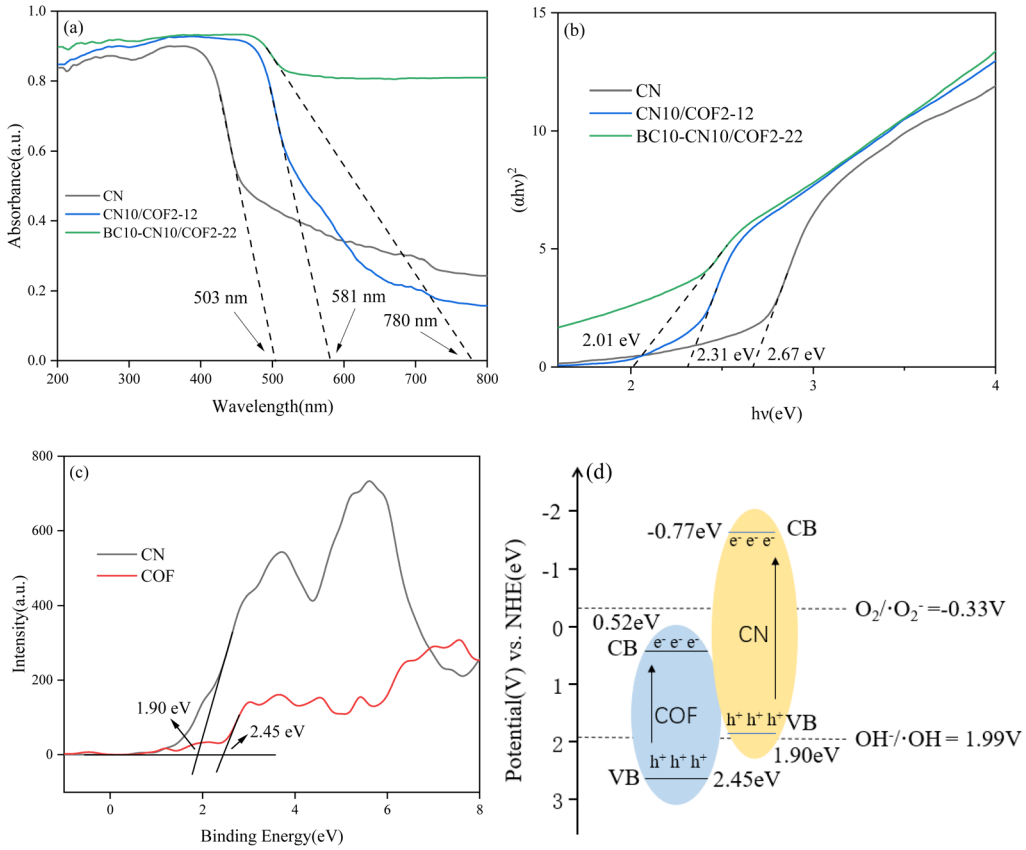

Fig. 6 Analysis of optical properties on photocatalysts: (a) UV-Vis spectra of CN, CN_{10}/COF_2-12, and BC_{10}–CN_{10}/COF_2-22. (b) Plot of $(ah\nu)^2$ *vs.* $h\nu$ for the band gap energy of CN, CN_{10}/COF_2-12, and BC_{10}–CN_{10}/COF_2-22. (c) Valence band XPS spectra of CN and COF. (d) Mechanism of CN_{10}/COF_2-12 composite photocatalyst.

XPS data indicate that the COF material has a higher valence band position (E_{VB} = 2.45 eV *vs.* 1.90 eV of CN), while CN shows a more negative conduction band energy level (E_{CB} = −0.77 eV *vs.* 0.52 eV of COF). The interlaced arrangement of energy bands in this heterojunction drives the photogenerated electrons in the CN conduction band to selectively recombine with the valence band holes of COF through the interface channel constructed by BC.[45] The Fermi level equilibrium at the BC_{10}–CN_{10}/COF_2-22 interface generates the upward band bending of CN and the downward band bending of COF, effectively reducing the apparent band gap of the composite material.

The photoluminescence (PL) spectra of heterojunction materials serve as an indicator of the separation efficiency of photogenerated electron–hole pairs. In general, a higher PL peak intensity correlates with a faster recombination rate of photogenerated electrons and holes in photocatalysts.[46] Fig. 7a illustrates the PL spectra of CN, CN_{10}/COF_2-12, and BC_{10}–CN_{10}/COF_2-22. Notably, CN exhibits a higher intensity of typical emission peaks at an excitation wavelength of 461 nm, suggesting rapid recombination of photogenerated e^-–h^+, which is the primary factor limiting its photocatalytic activity. This phenomenon may be attributed to the n–π* electron leaps.[47] The PL peak intensity of CN_{10}/COF_2-12 is significantly lower compared to CN, indicating that the heterojunction between CN and COF effectively suppresses the recombination of photogenerated e^-–h^+, facilitating an enhancement in photocatalytic activity. The PL peak intensity of BC_{10}–CN_{10}/COF_2-22 is observed to decrease further, indicating that the all-solid-state *Z*-scheme heterojunction more effectively inhibits the recombination of photogenerated e^-–h^+. The separation effect of photogenerated charges at the material interface is illustrated in Fig. 7b, with CN and COF exhibiting considerable impedance radii. In comparison to CN and COF, CN_{10}/COF_2-12 exhibits a reduced impedance radius, and BC_{10}–CN_{10}/COF_2-22 shows an even lower impedance radius, suggesting lower resistance and faster interfacial charge transfer.[48] These results demonstrate that heterojunctions, particularly all-solid-state *Z*-scheme heterojunctions, can enhance the separation efficiency of photogenerated carriers and accelerate the interfacial charge transfer, thereby facilitating the photocatalytic degradation of TC.

3.3 Mechanism of photocatalytic degradation

This study conducted capture experiments to identify the primary active species in the photocatalytic process. *P*-Benzoquinone (BQ), triethanolamine (TEOA), and isopropanol (IPA) at a concentration of 0.01 mol L^{-1} were utilized as trapping agents to eliminate $\cdot O_2^-$, h^+, and ·OH radicals, respectively, with the results depicted in Fig. 8. The degradation efficiency of TC in the system with the addition of BQ was found to be significantly

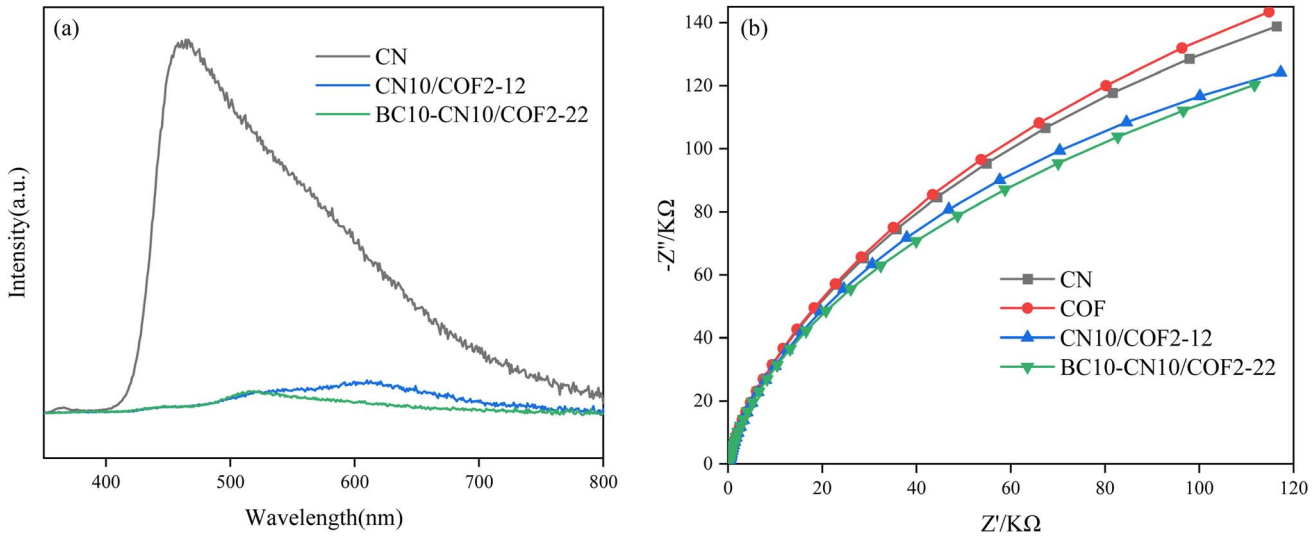

Fig. 7 Analysis of photogenerated charge carrier on photocatalysts: (a) photoluminescence of CN, CN_{10}/COF_2-12, and BC_{10}–CN_{10}/COF_2-22. (b) Electrochemical impedance spectroscopy of CN, COF, CN_{10}/COF_2-12, and BC_{10}–CN_{10}/COF_2-22.

reduced, reaching approximately 57% compared to the control without a trapping agent. In contrast, the addition of TEOA and IPA had a less pronounced effect, with TC degradation rates of 94.18% and 94.89%, respectively. The results demonstrate that $\cdot O_2^-$ radical played a pivotal role in the photocatalytic degradation of TC, while the contributions of h^+ and ·OH were comparatively less significant.

Xu *et al.*[49] proposed a classification of *Z*-scheme heterojunctions into three distinct categories: conventional *Z*-scheme heterojunctions, all-solid-state *Z*-scheme heterojunctions, and direct *Z*-scheme heterojunctions. In a conventional *Z*-scheme heterostructure, the photo-induced holes in the VB of the photocatalyst 1 are captured by the electron donor, while the photo-induced electrons in the CB of the photocatalyst 2 are absorbed by the electron acceptor.[50] In the all-solid-state *Z*-scheme heterostructure, upon light activation of the component photocatalysts, the light-induced electrons in the CB of photocatalyst 2 are transferred to the conducting material, subsequently reaching the VB of photocatalyst 1. Unlike other heterostructures, direct *Z*-scheme heterostructures do not involve a charge-transfer medium. Instead, the formation of charge complex is achieved through direct electron and hole transfer between the semiconductors.[51]

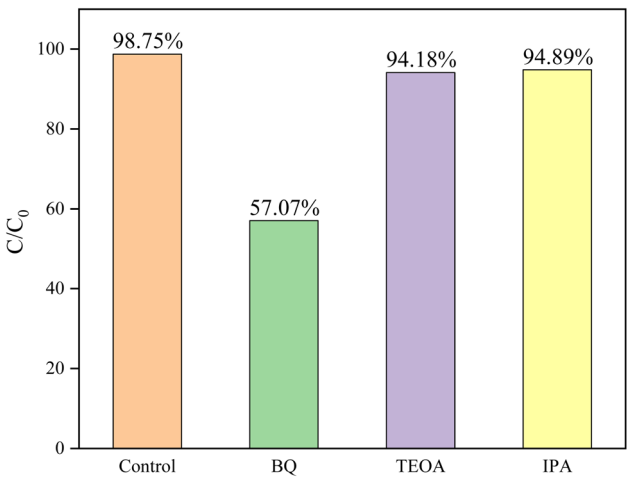

Fig. 8 Effect of different scavengers on the BC_{10}–CN_{10}/COF_2-22 photocatalytic degradation of TC.

This study elucidates the photo-induced charge transfer mechanism of the catalyst under visible light irradiation, highlighting the crucial role of the *Z*-scheme heterojunction in photocatalytic. The absorption edges of CN_{10}/COF_2-12 and BC_{10}–CN_{10}/COF_2-22 were obtained by UV-Vis spectroscopy, from which direct band gaps of 2.31 eV and 2.01 eV were calculated using the Tauc equation. The mechanism diagram is presented in Fig. 9. The CN_{10}/COF_2-12 heterostructure improves the photocatalytic efficiency. The all-solid-state *Z*-scheme heterostructure in BC_{10}–CN_{10}/COF_2-22 broadens the absorption spectrum of visible light, optimizes the separation efficiency of the photogenerated e^-–h^+ and inhibits their recombination effectively, thus improving the photocatalytic efficiency. Specifically, under visible light excitation, electrons transition from the conduction band of the COF to the valence band of the CN, while holes accumulating in the valence band of the COF and electrons in the conduction band of the CN. The migration of electrons and holes is facilitated by the electron mediator BC, which enhances the catalytic effect due to its high conductivity. Electrons accumulated on the CN conduction band are trapped by O_2, resulting in the generation of $\cdot O_2^-$. This is due to the fact that the CB edge potential of CN is lower than the standard $E^{\theta}(O_2/\cdot O_2^-)$ (−0.33 V *vs.* NHE). Simultaneously, the collective defects on the valence band of COF can oxidize OH^- to produce ·OH. This is due to the fact that the VB edge potential of COF is higher than the standard $E^{\theta}(\cdot OH/OH^-)$ (1.99 V *vs.* NHE). In conclusion, the BC-mediated all-solid-state *Z*-scheme heterojunction mechanism facilitates efficient carrier separation, the

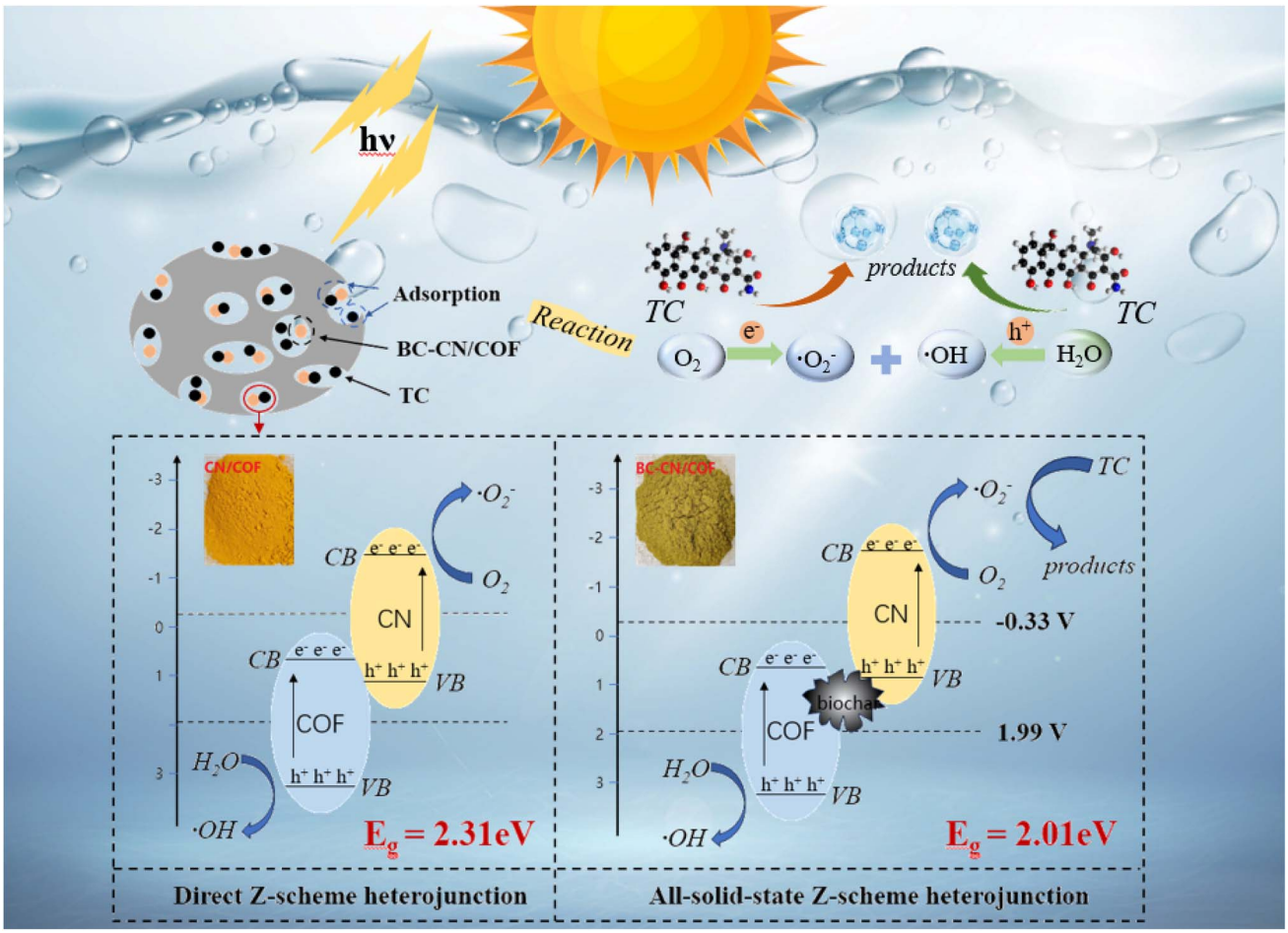

Fig. 9 Photocatalytic degradation mechanism of photocatalyst.

generation of reactive oxygen species, and an improvement in material stability, collectively enhancing the photocatalytic activity of BC_{10}–CN_{10}/COF_2-22.

4 Conclusion

This study successfully constructed a multifunctional heterojunction photocatalytic system for the efficient photocatalytic degradation of TC. Comparative experiments indicated that the optimal binary photocatalysts, CN_{10}/COF_2-12 achieved a TC degradation rate of 99.79% after 360 minutes of photocatalytic reaction, exhibiting 2.02-fold and 1.96-fold enhancement compared to individual components CN-10 and COF-2, respectively. The ternary all-solid-state *Z*-scheme heterojunction BC_{10}–CN_{10}/COF_2-22, constructed by further introducing BC, achieved a TC degradation rate of 99.65%, representing a 3.13-fold improvement over BC_{10}–CN_{10}-20. Radical trapping experiments revealed that $\cdot O_2^-$ was the primary active species with a contribution rate of 83.18% in the photocatalytic degradation of TC, while h^+ and ·OH played a less significant role. The BC-mediated all-solid-state *Z*-scheme heterojunction promotes efficient charge carrier separation, was the principal reason for the enhanced photocatalytic activity of BC_{10}–CN_{10}/COF_2-22. This study presents a novel approach for the photocatalytic degradation of TC, which is crucial for effective environmental remediation.

Data availability

The data used to support the findings of this study are available from the corresponding author upon request.

Author contributions

Qi Wei: experiments, data processing, writing-original draft. Baojun Yi (corresponding author): general framework, data processing, writing-review and editing, supervision, financial support. Zewen Hua: experiments, data processing. Zhengshuai Sun: data processing, writing-review and editing. Feng Guo: drawing, writing-reviewing and editing.

Conflicts of interest

The authors declare that they have no known competing financial interests or personal relationships that could have appeared to influence the work reported in this paper.

Acknowledgements

This work was supported by Key Research and Development Program of Hubei Province (2023BBB001), National Key Research and Development Program of China (2021YFD1600503), and Fundamental Research Funds for the Central Universities (2662024GXPY004).

References

1 Z. Sun, Q. Wei, W. Hua, M. Chen, Q. Yuan, B. Yi and Y. S. Ok, *J. Environ. Chem. Eng.*, 2024, **12**, 114290.
2 K. L. A. Cao, A. M. Rahmatika, Y. Kitamoto, M. T. T. Nguyen and T. Ogi, *J. Colloid Interface Sci.*, 2021, **589**, 252–263.
3 J.-Y. Zhang, C. Xia, H.-F. Wang and C. Tang, *J. Energy Chem.*, 2022, **67**, 432–450.
4 Y. Li, M. Fu, R. Wang, S. Wu and X. Tan, *Chem. Eng. J.*, 2022, **444**, 136567.
5 Ö. Hanay, B. Yıldız, S. Aslan and H. Hasar, *Environ. Sci. Pollut. Res.*, 2014, **21**, 3774–3782.
6 X. He, T. Kai and P. Ding, *Environ. Chem. Lett.*, 2021, **19**, 4563–4601.
7 M.-Q. Zhu and X.-F. Wang, *J. Phys. D: Appl. Phys.*, 2024, **57**, 335104.
8 J. Li, B. Huang, Q. Guo, S. Guo, Z. Peng, J. Liu, Q. Tian, Y. Yang, Q. Xu, Z. Liu and B. Liu, *Appl. Catal., B*, 2021, **284**, 119733.
9 J. E. Ellis, D. C. Sorescu, S. I. Hwang, S. C. Burkert, D. L. White, H. Kim and A. Star, *ACS Appl. Mater. Interfaces*, 2019, **11**, 41588–41594.
10 T. Su, Q. Shao, Z. Qin, Z. Guo and Z. Wu, *ACS Catal.*, 2018, **8**, 2253–2276.
11 J. Ran, W. Guo, H. Wang, B. Zhu, J. Yu and S.-Z. Qiao, *Adv. Mater.*, 2018, **30**, 1800128.
12 C. Yang, Z. Xue, J. Qin, M. Sawangphruk, S. Rajendran, X. Zhang and R. Liu, *J. Phys. Chem. C*, 2019, **123**, 4795–4804.
13 I. Papailias, N. Todorova, T. Giannakopoulou, N. Ioannidis, N. Boukos, C. P. Athanasekou, D. Dimotikali and C. Trapalis, *Appl. Catal., B*, 2018, **239**, 16–26.
14 C. Feng, J. Rong, Y. Zhang, X. Zheng, X. Li, S. Xu and Z. Li, *Appl. Catal., B*, 2023, **337**, 123005.
15 Y. Song, Q. Sun, B. Aguila and S. Ma, *Adv. Sci.*, 2019, **6**, 1970011.
16 S. Chandra, S. Kandambeth, B. P. Biswal, B. Lukose, S. M. Kunjir, M. Chaudhary, R. Babarao, T. Heine and R. Banerjee, *J. Am. Chem. Soc.*, 2013, **135**, 17853–17861.
17 H. Ran, Q. Xu, Y. Yang, H. Li, J. Fan, G. Liu, L. Zhang, J. Zou, H. Jin and S. Wang, *ACS Catal.*, 2024, **14**, 11675–11704.
18 M. Luo, Q. Yang, K. Liu, H. Cao and H. Yan, *Chem. Commun.*, 2019, **55**, 5829–5832.
19 J. Wang, Y. Yu, J. Cui, X. Li, Y. Zhang, C. Wang, X. Yu and J. Ye, *Appl. Catal., B*, 2022, **301**, 120814.
20 Y. Liu, Y. Zhu, S. B. Alahakoon and E. Egap, *ACS Mater. Lett.*, 2020, **2**, 1561–1566.
21 Q. Wang, J. Wang, J.-C. Wang, X. Hu, Y. Bai, X. Zhong and Z. Li, *ChemSusChem*, 2021, **14**, 1131–1139.
22 H. Li, W. Tu, Y. Zhou and Z. Zou, *Adv. Sci.*, 2016, **3**, 1500389.
23 X. Wu, J. Zhao, L. Wang, M. Han, M. Zhang, H. Wang, H. Huang, Y. Liu and Z. Kang, *Appl. Catal., B*, 2017, **206**, 501–509.
24 Y. Liu, Y. Yuan, S. Ni, J. Liu, S. Xie and Y. Liu, *Water Sci. Technol.*, 2022, **85**, 2639–2651.
25 D. Jiang, W. Ma, P. Xiao, L. Shao, D. Li and M. Chen, *J. Colloid Interface Sci.*, 2018, **512**, 693–700.
26 J. Zou, J. Liu, Y. Xie, G. Peng, L. Duan, D. Hu, S. Chen, F. Qu and L. Lu, *Chem. Eng. J.*, 2023, **468**, 143849.
27 W. Xiang, X. Zhang, J. Chen, W. Zou, F. He, X. Hu, D. C. W. Tsang, Y. S. Ok and B. Gao, *Chemosphere*, 2020, **252**, 126539.
28 C. Ma, Y. Zhang, B. Yin, J. F. Chen, M. H. Guo and X. Gao, *J. Environ. Chem. Eng.*, 2023, **11**, 109135.
29 Q. Tang, Q. Cheng and Z. Pan, *Sustainable Mater. Technol.*, 2024, **41**, e01115.
30 L. Xiao, S. Zhang, B. Chen, P. Wu, N. Feng, F. Deng and Z. Wang, *J. Environ. Chem. Eng.*, 2023, **11**, 109693.
31 A. Thomas, A. Fischer, F. Goettmann, M. Antonietti, J.-O. Müller, R. Schlögl and J. M. Carlsson, *J. Mater. Chem.*, 2008, **18**, 4893–4908.
32 K. Dey, M. Pal, K. C. Rout, S. Kunjattu H, A. Das, R. Mukherjee, U. K. Kharul and R. Banerjee, *J. Am. Chem. Soc.*, 2017, **139**, 13083–13091.
33 M. Zebardast, A. F. Shojaei and K. Tabatabaeian, *Iran. J. Catal.*, 2018, **8**, 297–309.
34 X. Du, G. Zou, Z. Wang and X. Wang, *Nanoscale*, 2015, **7**, 8701–8706.
35 Q. Zhao, B. Zhao, X. Long, R. Feng, M. Shakouri, A. Paterson, Q. Xiao, Y. Zhang, X.-Z. Fu and J.-L. Luo, *Nano-Micro Lett.*, 2024, **16**, 80.
36 M.-Y. Zhang, J.-K. Li, R. Wang, S.-N. Zhao, S.-Q. Zang and T. C. W. Mak, *Adv. Sci.*, 2021, **8**, 2101884.
37 J. Du, Z. Xu, H. Li, H. Yang, S. Xu, J. Wang, Y. Jia, S. Ma and S. Zhan, *Appl. Surf. Sci.*, 2021, **541**, 148487.
38 K. Qi, M. Song, X. Xie, Y. Wen, Z. Wang, B. Wei and Z. Wang, *Chemosphere*, 2022, **287**, 132192.
39 Y.-N. Zang, S.-S. Yang, J. Ding, S.-Y. Zhao, C.-X. Chen, L. He and N.-Q. Ren, *RSC Adv.*, 2021, **11**, 15106–15117.
40 H. Dai, H. Li and Q. Yang, *Microporous Mesoporous Mater.*, 2022, **342**, 112121.
41 Z. Tan, J. Zou, L. Zhang and Q. Huang, *J. Mater. Cycles Waste Manage.*, 2018, **20**, 1036–1049.
42 Q. Xue, B. Song, Q. Feng, Z. Yu, K. Hu, Y. Yang and X. Shen, *Appl. Surf. Sci.*, 2024, **645**, 158869.
43 D. Jiang, T. Wang, Q. Xu, D. Li, S. Meng and M. Chen, *Appl. Catal., B*, 2017, **201**, 617–628.
44 H. Zhang, L.-c. Nengzi, X. Li, Z. Wang, B. Li, L. Liu and X. Cheng, *Chem. Eng. J.*, 2020, **386**, 124011.
45 Y. Yao, Y. Hu, H. Hu, L. Chen, M. Yu, M. Gao and S. Wang, *J. Colloid Interface Sci.*, 2019, **554**, 376–387.

46 J. Yu, S. Wang, J. Low and W. Xiao, *Phys. Chem. Chem. Phys.*, 2013, **15**, 16883–16890.
47 S. Zhang, X. Rong, T. Sun, P. Gao, J. Liu, X. Qiu, X. Zhou and Z. Wu, *Diamond Relat. Mater.*, 2023, **138**, 110167.
48 F.-J. Zhang, F.-Z. Xie, S.-F. Zhu, J. Liu, J. Zhang, S.-F. Mei and W. Zhao, *Chem. Eng. J.*, 2013, **228**, 435–441.
49 Q. Xu, L. Zhang, J. Yu, S. Wageh, A. A. Al-Ghamdi and M. Jaroniec, *Mater. Today*, 2018, **21**, 1042–1063.
50 K. Maeda, *ACS Catal.*, 2013, **3**, 1486–1503.
51 I. J. Ani, U. G. Akpan, M. A. Olutoye and B. H. Hameed, *J. Cleaner Prod.*, 2018, **205**, 930–954.